HHS Public Access

Author manuscript

Exp Eye Res. Author manuscript; available in PMC 2021 November 01.

Published in final edited form as:

Exp Eye Res. 2020 November ; 200: 108202. doi:10.1016/j.exer.2020.108202.

IOP-induced regional displacements in the optic nerve head and correlation with peripapillary sclera thickness

Yanhui Ma[1], **Sunny Kwok**[1], **Jiajun Sun**[1], **Xueliang Pan**[2], **Elias Pavlatos**[1], **Keyton Clayson**[1,3], **Nicholas Hazen**[1,3], **Jun Liu**[1,3,4,*]

[1]Department of Biomedical Engineering, Ohio State University, Columbus, Ohio

[2]Department of Biomedical Informatics, Ohio State University, Columbus, Ohio

[3]Biophysics Interdisciplinary Group, Ohio State University, Columbus, Ohio

[4]Department of Ophthalmology and Visual Science, Ohio State University, Columbus, Ohio

Abstract

Mechanical insult induced by intraocular pressure (IOP) is likely a driving force in the disease process of glaucoma. This study aimed to evaluate regional displacements in human optic nerve head (ONH) and peripapillary tissue (PPT) in response to acute IOP elevations, and their correlations with morphological characteristics of the posterior eye. Cross-sectional (2D) images of the ONH and PPT in 14 globes of 14 human donors were acquired with high-frequency ultrasound during whole globe inflation from 5 to 30 mm Hg. High-frequency ultrasound has a spatial resolution of tens of micrometers and is capable of imaging through the ONH and PPT thickness. Tissue displacements were calculated using a correlation-based speckle tracking algorithm for a dense matrix of kernels covering the 2D imaging plane. The ONH was manually segmented in the ultrasound B-mode images acquired at 5 mmHg based on echogenicity. The lamina cribrosa (LC) boundaries were visible in eight of the fourteen eyes and the LC region was segmented using a semi-automated superpixel-based method. The ONH had larger radial displacement than the PPT in all tested eyes and the difference increased with increasing IOP. A significant negative correlation was found between ONH-PPT displacement difference and PPT thickness ($p<0.05$), while no significant correlations were found between ONH-PPT displacement difference and other morphological parameters including PPT radius of curvature, scleral canal size, LC thickness and anterior LC surface depth. Within the ONH, the radial displacement decreased in the region anterior to and across LC but not in the region posterior to LC. Finite element models using simplified geometry and material properties confirmed the role of LC in reducing the overall ONH radial displacements, but did not predict the displacement gradient change observed experimentally. These results suggested that a thinner PPT may be associated with a larger relative posterior motion of the ONH with respect to the surrounding PPT and the LC

[*]**Correspondence**: Jun Liu, Ph.D., 270 Bevis Hall, 1080 Carmack Rd, Columbus OH; Phone: 614-247-8904; Fax: 614-292-7301; liu.314@osu.edu.

may play a major role in preventing excessive posterior displacement of ONH at acute IOP elevations.

Keywords

biomechanics; optic nerve head; lamina cribrosa; displacement; ultrasound elastography; peripapillary tissue; glaucoma

1. Introduction

Intraocular pressure (IOP) is strongly associated with glaucoma onset and progression. Glaucomatous axonal damage initiates at the optic nerve head (ONH) (Quigley et al., 1981; Nickells et al., 2012), and the biomechanical responses of the ONH to IOP elevation are likely important for determining glaucoma susceptibility (Burgoyne et al., 2005; Campbell et al., 2014).

The ONH is structurally complex and composed of different types of tissues. Many advanced imaging methods have been applied to visualize the ONH and quantify its deformation. These methods include 3D histomorphometry (Yang et al., 2009), confocal microscopy (Albon et al., 2000), micro-computed tomography (μCT) (Coudrillier et al., 2016), second harmonic generation (SHG) imaging (Midgett et al., 2017; Sigal et al., 2014) and optical coherence tomography (OCT) (Fazio et al., 2018; Girard et al., 2016; Wang et al., 2017; Wei et al., 2018). Our laboratory has developed a high-frequency (50–55 MHz) ultrasound elastography technique to quantify the deformation of ocular tissue, including the cornea (Clayson et al., 2020, 2017; Pavlatos et al., 2018a), the sclera (Pavlatos et al., 2016; Perez et al., 2016), and the ONH (Ma et al., 2020, 2019; Pavlatos et al., 2018b). High-frequency ultrasound allows imaging of the ONH during whole globe inflation testing, which reduces non-physiological stress concentrations induced by tissue clamping (Whitford et al., 2016). More importantly, high-frequency ultrasound has a better penetration depth (1–2 mm) compared to optical methods (hundreds of micrometers), and is capable of imaging through the entire thickness of both the ONH and the peripapillary tissue (PPT). The spatial resolution (~30 μm vertically and ~60 μm horizontally) is adequate to differentiate the peripapillary sclera and the optic nerve tissue, and in many scanned eyes, the lamina cribrosa (LC). The displacement sensitivity based on radiofrequency (RF) analysis with interpolation is much higher compared to image-based analysis, reaching tens of nanometers.

Using 2D high-frequency ultrasound imaging and elastography, we have reported the deformation of the ONH and PPT in human donor eyes, showing a depth-dependent compression concentrated in the anterior ONH and a higher shear in the vicinity of the ONH-PPT border (Ma et al., 2019). We also observed a larger vertical displacement of the ONH as compared to PPT. In this study, we performed further analyses of the 2D displacement data acquired in the previous study. Specifically, we computed and quantified the radial displacements, i.e., the displacement along the globe radii during IOP elevation from 5 to 30 mm Hg to answer two sets of questions: (1) How do the ONH and the PPT radial displacements differ during IOP elevation and how does the displacement difference correlate with morphological characteristics of the posterior eyes? (2) How does radial

displacement vary through depth within the ONH and how does the variation relate to the location of LC? These studies aimed to gain further insights into the mechanical responses of the tissues within and around the ONH in relation to IOP elevation, and to better understand the roles of the load-bearing tissues such as the PPT and the LC in affecting ONH biomechanics.

2. Methods

2.1 Donor globe preparation and experimental setup

Fourteen globes from 14 human donors without documented ocular diseases or surgeries were obtained from the Lion's Eye Bank of West Central Ohio (Dayton, OH, USA) in accordance with the Declaration of Helsinki (age range: 20–75 years; mean ± SD: 44 ± 17 years; 12 Caucasian and 2 African American; 9 male and 5 female). All globes were recovered within 12 hours postmortem and were tested at room temperature within 36 hours postmortem. The globes were stored in a moist container at 4°C until experimental use. The optic nerve was trimmed close to the surface of the sclera for ultrasound imaging from the posterior side (Figure 1A). Two spinal needles were inserted near the equator of the globe to secure the eye to a custom-built holder. Two 20G needles were inserted into the anterior chamber of the eye, one connected to a programmable syringe pump (PhD Ultra; Harvard Apparatus, Holliston, MA, USA) to control IOP, and the other connected to a pressure sensor (P75; Harvard Apparatus, Holliston, MA, USA) to continuously record IOP. The eye was immersed in 0.9% saline to maintain tissue hydration and facilitate ultrasound transduction.

2.2 Inflation testing with ultrasound data acquisition

The globes were first preconditioned with 20 IOP cycles from 5 to 30 mm Hg at 2 seconds per cycle before equilibrating at 5 mm Hg for 30 minutes. The inflation tests were then performed by increasing IOP from 5 to 30 mm Hg with 0.5 mm Hg steps. The IOP was held constant at each IOP level for 30 seconds before ultrasound scans were acquired. Seven donor globes were scanned by using the ultrasound probe RMV55 (Vevo 660; VisualSonics, Inc., Toronto, Ontario, Canada) and seven additional globes were scanned by using the ultrasound probe MS700 (Vevo 2100; VisualSonics, Inc.). It is noted that these two ultrasound imaging systems gave similar displacement measurements (Ma et al., 2019). Cross-sectional images were acquired along the nasal-temporal meridian of the ONH with an image width of 8 mm from Vevo 660 ultrasound system and 9.73 mm from Vevo 2100. For all inflation testing, control of the testing apparatus and data acquisition were implemented using a customized LabView program (National Instruments, Austin, TX, USA).

2.3 Ultrasound speckle tracking for calculating displacements

The ultrasound speckle tracking algorithms have been described and validated previously (Ma et al., 2020; Pavlatos et al., 2018a; Perez et al., 2016; Tang and Liu, 2012). In brief, during ultrasound scanning, RF data which are the digitized voltage values of the received ultrasound signal, were acquired and stored as A-lines with 19 μm intervals in the direction perpendicular to sound propagation (horizontal). Within each A-line, the RF data were

sampled at approximately 1.5 μm intervals in the direction of ultrasound wave propagation (vertical). A region of interest (ROI) was defined within the scanned area at the reference/initial IOP by fitting two concentric circles that matched approximately the inner and outer surfaces of the PPT. The difference in the radii of the two fitted circles was used to estimate the thickness of PPT. The average of the two radii was used as the PPT radius of curvature. The shared center of the two fitted circles was used for radial displacement calculation from the measured vertical and horizontal displacements (Figure 1B). The retina was largely excluded from the ROI, while the choroid was difficult to separate in the ultrasound images from the sclera and thus included. Within the ROI, the RF data were divided into kernels, each containing 51 × 31 pixels (vertical × horizontal), or approximately 75 μm × 570 μm in size with 50% overlap (Tang and Liu, 2012). To compute the displacements of each kernel, the normalized cross-correlation coefficient was used to evaluate the similarity of the kernels in successive images within a search window. The maximum correlation coefficient value indicated the best match and the center of the kernel was designated as the new location of the kernel. Spline interpolation was used to achieve subpixel resolution in displacement tracking. The vertical and horizontal displacements of each kernel were calculated cumulatively with respect to its location at the initial IOP. Radial displacement was calculated as (vertical displacement × $sin\theta$ + horizontal displacement × $cos\theta$), where θ is the angle between the Cartesian and spherical coordinate systems at each kernel (Figure 1B). The radial displacement calculation eliminates the effect of pure rotation and also better coincides with the anatomy of the posterior eye.

2.4 Regional segmentation and morphometric analysis

As described above, the inner and outer surfaces of the PPT and ONH were determined by two concentrically fitted circles of the ROI. The border between the ONH and the PPT was manually delineated based on differences in signal intensity in the cross-sectional ultrasound B-mode image (Figure 2A). The PPT contains primarily the peripapillary sclera (PPS) on both side of the ONH within the ultrasound scan (up to 5 mm from the center of the ONH), and potentially the choroid, pia mater, and dura mater if they were included in the ROI. These tissue structures are much smaller than PPS; therefore, the mechanical response of the PPT should be predominantly that of the PPS. To evaluate the interobserver repeatability of the manual segmentation between ONH and PPT, three experienced observers were asked to segment five images independently. The regional displacements (averaged over all kernels within each region) were calculated and compared, which showed excellent interobserver repeatability (Cronbach Coefficient $\alpha > 0.99$), and the manual segmentation was thus adopted. Segmentation by one observer on all 14 eyes was used for further analysis. The Bruch's membrane opening (BMO) termination points were also manually marked on the B-mode images, and the length of the line connecting the two BMO termination points was defined as scleral canal size.

In eight out of fourteen ultrasound images, the LC was visible with a brighter echogenicity than the neural tissue within the ONH, likely due to the collagenous component within the LC. The LC was segmented in these scans using a semi-automated method. First, a simple linear iterative clustering (SLIC) algorithm (Achanta et al., 2012) was used to decompose the image into superpixels which are image patches consisting of pixels with similar

brightness, as shown in Figure 2B. Superpixels belonging to the LC were then manually selected, and the continuous area composed of selected superpixels was designated as the LC.

The anterior LC surface depth (ALCSD) was calculated as the mean perpendicular distance from three points on the ALCS to the BMO reference plane (Figure 2C). These three points are at 1/3, ½ and 2/3 width of the LC. LC thickness was quantified as the mean distance from the same three equi-spaced points on the anterior LC surface as identified for ALCSD measurement, to their corresponding points on the posterior LC surface. It is noted that all morphometric measurements were performed on RF data which had higher pixel resolution than B-mode ultrasound images.

The ONH-PPT displacement difference was calculated as the difference between the displacement of the ONH averaged over all kernels within a donor's ONH including LC and that of the PPT averaged over all kernels within a donor's PPT. Pearson correlations between ONH-PPT displacement difference and several parameters, including ONH displacement, PPT displacement, PPT thickness, PPT radius of curvature, scleral canal size, ALCSD, LC thickness, and age, were evaluated.

A vertical column of kernels at the center of the ONH was selected from all scanned eyes. The radial displacements of the kernels in this column were plotted against their location to evaluate the anterior to posterior variation. For the eight eyes whose LCs were segmented, kernels belonging to the LC were marked to evaluate the correspondence between LC location and displacement variation within the ONH.

2.5 Finite element (FE) simulation of ONH displacements with or without LC

FE models were used to generate displacement data in spherical thin shell structures after applying a pressure of 25 mmHg to the inner surface (corresponding to the experimental change of IOP from 5 to 30 mmHg). A uniform thickness of 0.9 mm and an internal radius of curvature of 12.0 mm were used, following the typical dimensions of human posterior sclera. An inclusion of 1.4 mm in width was introduced at the top of the scleral shell to simulate the ONH. The middle third layer of the ONH was assigned with a different modulus to simulate the LC. All materials were assumed isotropic, homogeneous, and near-incompressible. Baseline literature values were used for sclera, ONH neural tissue, and LC moduli, which were 3, 0.03, and 0.3 MPa, respectively (Sigal et al., 2005). The models were built and meshed with eight-node structural solid element (SOLID185, Ansys Inc, PA). A mesh convergence study was conducted to optimize the simulation efficiency and accuracy. A mesh with 32,250 elements was chosen. One eighth of the sphere was modeled with assumption of axi-symmetry. The radial displacements were calculated and compared for three models: uniform scleral shell, scleral shell with ONH but not LC, scleral shell with ONH and LC.

3. Results

Various human ONH morphologies were seen in high-resolution ultrasound images, with different PPT thickness, scleral canal size, LC thickness and location, and ONH orientation

(Figure 3). The radial displacement maps calculated from ultrasound speckle tracking are shown in Figure 4, displaying regional variations between and within the ONH and the PPT. The descriptive statistics of morphological parameters are tabulated in Table 1, including the range and mean value of PPT thickness, PPT radius of curvature, scleral canal size, LC thickness, and ALCSD.

3.1 ONH-PPT displacement difference

The radial displacements of the ONH and the PPT increased nonlinearly with increasing IOP (Figure 5A). The ONH displaced more outward than the PPT at every IOP level (all $p < 0.001$), while the displacements of the two regions were highly correlated (Pearson correlation $R > 0.95$ at all IOP levels). At 30 mmHg, the average radial displacement of the ONH and PPT were 110.5 ± 43.7 μm and 65.1 ± 36.5 μm, respectively. ONH-PPT displacement difference, defined as the difference in the average radial displacements between ONH and PPT, increased with increasing IOP (26.2 ± 7.6 μm at 15 mm Hg; 45.4 ± 13.7 μm at 30 mm Hg). The ONH-PPT displacement difference was correlated with the radial displacement of the ONH at all pressure levels (all R's > 0.64, p's < 0.05), but not that of the PPT (p's > 0.05).

The ONH-PPT displacement difference was negatively correlated with PPT thickness (R = −0.59, −0.57, −0.55; p = 0.026, 0.033, 0.041 at IOP = 10, 20, 30 mm Hg, respectively, Figure 5B). Age was also negatively correlated with PPT thickness (R = −0.57, p = 0.033, Figure 5C). ONH-PPT displacement difference was not correlated with age (R = 0.02, 0.04, 0.06; p = 0.94, 0.89, 0.84 at IOP = 10, 20, 30 mm Hg, respectively). The Pearson correlation coefficients between morphological parameters (i.e., PPT thickness, PPT radius, canal size, LC thickness, and ALCSD) and displacement quantifications (i.e., ONH displacement, PPT displacement, and ONH-PPT displacement difference at 30 mmHg) are tabulated in Table 1. Significant correlation was only observed between PPT thickness and ONH-PPT displacement difference.

3.2 LC location and displacement variation through thickness

The radial displacements of the kernels of the central vertical column within the ONH of all tested eyes are shown in Figure 6A. In eight of the fourteen tested donor eyes, where the LC was segmented out using the superpixel method, a consistent pattern of radial displacement was observed: the radial displacement curve exhibited a negative slope anterior to the LC and a close to zero or slightly positive slope posterior to the LC. Within the LC region, the slope could be negative, close to zero, or transitioning from negative to close to zero (Figure 6A). The radial displacement of the kernels in all vertical columns within the ONH of a representative donor eye was plotted in Figure 6B to illustrate the displacement profiles from nasal to temporal ONH. A similar pattern was seen in the displacement profiles across the width of the ONH.

FE models of human posterior eye showed that radial displacements had a constant gradient through tissue thickness for a uniform scleral shell (Figure 7). In comparison, inclusion of an ONH with a much lower modulus would predict much higher radial displacements within the ONH. The presence of LC within the ONH, with a modulus between that of the neural

tissue of the ONH and the sclera, reduced the radial displacements of the ONH significantly. However, the simple FE models did not reproduce the trends of radial displacement gradient change observed experimentally (as shown in Figure 6).

4. Discussion

A high-frequency ultrasound speckle tracking technique was used to map and quantify 2D radial displacements of the human posterior eye in response to IOP elevation. With a greater penetration than achievable with optical imaging, this technique allows us to visualize the posterior ocular shell through the full thickness and to investigate the depth-dependent mechanical behavior of the ONH. The wide field of view allowed us to simultaneously acquire measurements of the ONH and the PPT during whole globe inflation and to identify the differences and correlations in their mechanical responses. The primary findings of this study are as follows:

1. At an acute IOP increase, the ONH-PPT displacement difference was negatively correlated with the PPT thickness at every IOP level (Figure 5B).
2. Through the depth of the ONH, radial displacement decreased in the region anterior to and across LC but plateaued (with a small increase) in the region posterior to LC (Figure 6), indicating a significant role LC may play in reducing ONH radial displacement (Figure 7).

The ONH displaced more posteriorly than the PPT at an acute IOP rise in all tested eyes. This was consistent with previous reports from computational studies (Sigal et al, 2011a; Sigal et al, 2011b) and experiments on perfusion fixed monkey eyes (Yang et al, 2009) and ex vivo inflation testing of porcine (Coudrillier et al, 2016; Pavlatos et al, 2018b) and human donor eyes (Fazio et al, 2016; Behkam et al, 2019; Midgett et al, 2020). The ONH-PPT displacement difference was found to negatively correlate with PPT thickness. Since PPT thickness was also found to negatively correlate with age, we performed multivariate analysis and found that the negative association between ONH-PPT displacement difference and PPT thickness remained significant after adjusted for the age effect using either partial correlation coefficient analysis ($R=-0.68$, $p=0.007$) or multivariate linear regression analysis ($p=0.01$). Scleral thickness was ranked the 5th most important determinants of ONH biomechanics, following the stiffness of the sclera, the size of the eye, IOP, and the stiffness of the LC, based on computational models encompassing 21 factors representing generic ONH geometry and material properties (Sigal et al., 2005). It was predicted that independently increasing either the stiffness or thickness of the sclera could reduce strains in the ONH (Sigal et al., 2009). Whole globe models combining specimen-specific corneoscleral shells and generic ONHs were developed and showed that scleral thickness was the largest determinant of ONH biomechanics among the geometrical factors of the eye (Norman et al., 2011). Our experimental results showed an interesting relationship between PPT thickness and the difference between the overall ONH and PPT radial displacements. Assuming that the PPT thickness measured in this study was primarily determined by the peripapillary sclera thickness, our results provide additional insights into a thin sclera's detrimental effect on IOP related mechanical insult at the ONH. The relative outward displacement of the ONH with respect to the PPT likely creates a localized stretch of the

retinal ganglion cell (RGC) axon segments within the ONH as the axons course from the peripapillary region to the scleral canal. A thin sclera was associated with a larger ONH-PPT displacement difference, which may underlie the higher glaucoma susceptibility in normal tension glaucoma and myopia, which tend to have thinner sclera (Jonas and Xu, 2014; Park et al., 2014). It has also been reported that the sclera thins with age in monkeys (Girard et al., 2009), mice (Nguyen et al., 2013), dogs (Palko et al., 2016), and humans (Coudrillier et al., 2012). In the current study, we also found a negative correlation between PPT thickness and age in the tested donor eyes (Figure 5C). No correlation was found between ONH-PPT displacement difference and age, possibly due to the limited sample size in this study. We also did not find significant correlations between ONH-PPT displacement difference and PPT radius, scleral canal size, LC thickness, and ALCSD, while the mean and range of these parameters (Table 1) were consistent with those cited in computational models (Sigal et al, 2005) and in vivo OCT measurements of normal human eyes (Park et al, 2012; Seo et al, 2014). Future studies are needed to evaluate the association of these parameters with ONH and PPT displacements in a larger sample size.

Our results revealed a depth-dependent variation of the radial displacements within the ONH. In most tested eyes, radial displacement was highest in the anterior ONH, steadily decreased until reaching to and across the LC, and then plateaued in the posterior ONH (Figure 6). This pattern was curiously similar to that of the optic nerve tissue pressure from anterior to posterior ONH measured by micropipettes in dog eyes in vivo (Morgan et al, 1995): an initial drop in the anterior until across LC and plateau in the region further posterior, suggesting a possible correspondence between tissue pressure and displacement. This pattern indicates a biomechanical role that the LC may play and is not immediately apparent; that is, the LC prevents excessive outward displacement of the ONH during IOP elevation, especially rapid and large elevations such as those seen in eye rubbing or head inversion (Eisenlohr et al., 1962; Turner et al., 2019; Weinreb et al., 1984). This role of LC in reducing posterior displacement of the ONH was confirmed in our FE simulations (Figure 7), although these simplified models did not reproduce the gradient change around LC observed in the experimental data. Further computational studies are needed to investigate what tissue material or geometrical properties would predict the experimental outcome. Posterior displacements of the ONH in response to IOP elevation has been reported in other animals such as rodents (Nguyen et al, 2013). Although rodents do not have a collagenous LC, the astrocytic lamina may fulfill a similar function in eyes with a much smaller scleral canal. In a rat model with experimentally induced glaucoma, ONH astrocyte actin fibers re-orientated to the longitudinal axis of the axons (Tehrani et al., 2014), which may indicate a response to the excessive posterior displacement of the ONH upon IOP rise.

The displacement gradient also appeared to change from anterior to posterior ONH (Figure 6). Displacement gradient in the radial direction is radial strain, whose spatial variations (i.e., strain maps) have been reported in our previous study (Ma et al, 2019). For the eight eyes whose LCs were identified, we plotted the radial strain curve to examine how it varied from anterior to posterior LC in the central ONH (Figure 8). In all eyes, compressive (negative) strain was largest in the anterior LC and decreased across LC. In four eyes, radial strain became positive in the posterior LC. The mechanism for a positive radial strain in the posterior LC was unclear, but this result was consistent with a previous study using phase-

contrast μCT and digital volume correlation that showed a volume increase in the posterior LC at IOP elevation possibly due to fluid flow from anterior to posterior LC (Coudrillier et al, 2016).

This study has a few limitations. First, ex vivo testing could not fully represent the in vivo configuration, including the absence of CSFP, central retinal artery blood pressure, and tension on the optic nerve. Computational and ex vivo experimental studies have shown that the effect of these pressures was mostly concentrated in regions posterior to LC (Feola et al., 2016, 2017). How these pressures influence ONH deformation in vivo is still unknown. Second, not all ultrasound images obtained in this study had clearly identifiable LCs in the scanned eyes. Ultrasound imaging is non-destructive and histological analysis can be performed in the same eye after ultrasound scanning. Future studies will corroborate LC location and thickness identified from ultrasound images with histomorphometry. Third, the current 2D method does not provide the full 3D analysis of the mechanical response in the human posterior eye. We have implemented and validated a 3D ultrasound speckle tracking technique to quantify the deformation in porcine ONH (Ma et al., 2020; Pavlatos et al., 2016; Perez et al., 2016). Future studies will evaluate the 3D variations, including width-, depth- and quadrant- dependent variations in ONH mechanical response to IOP.

In conclusion, high-frequency ultrasound speckle tracking allows simultaneous quantification of the biomechanical responses of the ONH and PPT through full tissue thickness. We found that the ONH-PPT displacement difference was larger in eyes with thinner PPT, possibly linked to the higher glaucoma risk in eyes with thinner sclera. LC likely plays an important role in limiting the posterior displacement of the ONH, besides being a structural support for RGC axons. An understanding of the spatial variation of tissue displacements in correspondence to tissue structure and geometry may provide new insights into how IOP-induced mechanical insults relate to clinically observed patterns of structural and functional changes in glaucoma.

Acknowledgments

This study was supported in part (Vevo2100 equipment use) by National Institutes of Health (NIH; Bethesda, MD, USA) grant R01EY025358.

Grant Support: NIH R01EY025358

References

Achanta R, Shaji A, Smith K, Lucchi A, Fua P, Süsstrunk S, 2012 SLIC superpixels compared to state-of-the-art superpixel methods. IEEE Trans. Pattern Anal. Mach. Intell 34, 2274–2282. [PubMed: 22641706]

Albon J, Purslow PP, Karwatowski WSS, Easty DL, 2000 Age related compliance of the lamina cribrosa in human eyes. Br. J. Ophthalmol 84, 318–323. [PubMed: 10684845]

Behkam R, Kollech HG, Jana A, Hill A, Danford F, Howerton S, Ram S, Rodríguez JJ, Utzinger U, Girkin CA, Vande Geest JP, 2019 Racioethnic differences in the biomechanical response of the lamina cribrosa, Acta Biomater 88:131–140. [PubMed: 30797107]

Burgoyne CF, Downs JC, Bellezza AJ, Suh J-KF, Hart RT, 2005 The optic nerve head as a biomechanical structure: a new paradigm for understanding the role of IOP-related stress and strain in the pathophysiology of glaucomatous optic nerve head damage. Prog. Retin. Eye Res 24, 39–73. [PubMed: 15555526]

Campbell IC, Coudrillier B, Ethier CR, 2014 Biomechanics of the posterior eye: a critical role in health and disease. J. Biomech. Eng 136, 21005.

Clayson K, Pavlatos E, Ma Y, Liu J, 2017 3D Characterization of corneal deformation using ultrasound speckle tracking. J. Innov. Opt. Health Sci 10, 1742005. [PubMed: 29399203]

Clayson K, Pavlatos E, Pan X, Sandwisch T, Ma Y, Liu J, 2020 Ocular Pulse Elastography: Imaging Corneal Biomechanical Responses to Simulated Ocular Pulse Using Ultrasound. Translational Vision Science and Technologies 9 (1), 5. doi:10.1167/tvst.9.1.5.

Coudrillier B, Geraldes DM, Vo NT, Atwood R, Reinhard C, Campbell IC, Raji Y, Albon J, Abel RL, Ethier CR, 2016 Phase-contrast micro-computed tomography measurements of the intraocular pressure-induced deformation of the porcine lamina cribrosa. IEEE Trans. Med. Imaging 35, 988–999. [PubMed: 26642429]

Coudrillier B, Tian J, Alexander S, Myers KM, Quigley HA, Nguyen TD, 2012 Biomechanics of the human posterior sclera: age-and glaucoma-related changes measured using inflation testing. Invest. Ophthalmol. Vis. Sci 53, 1714–1728. [PubMed: 22395883]

Eisenlohr JE, Langham ME, Maumenee AE, 1962 Manometric studies of the pressure--volume relationship in living and enucleated eyes of individual human subjects. Br. J. Ophthalmol 46, 536. [PubMed: 18170811]

Fazio MA, Johnstone JK, Smith B, Wang L, Girkin CA, 2016 Displacement of the Lamina Cribrosa in Response to Acute Intraocular Pressure Elevation in Normal Individuals of African and European Descent, Invest Ophthalmol Vis Sci 57(7):3331–9. [PubMed: 27367500]

Fazio MA, Clark ME, Bruno L, Girkin CA, 2018 In vivo optic nerve head mechanical response to intraocular and cerebrospinal fluid pressure: imaging protocol and quantification method. Sci. Rep 8, 12639. [PubMed: 30140057]

Feola AJ, Coudrillier B, Mulvihill J, Geraldes DM, Vo NT, Albon J, Abel RL, Samuels BC, Ethier CR, 2017 Deformation of the lamina cribrosa and optic nerve due to changes in cerebrospinal fluid pressure. Invest. Ophthalmol. Vis. Sci 58, 2070–2078. [PubMed: 28389675]

Feola AJ, Myers JG, Raykin J, Mulugeta L, Nelson ES, Samuels BC, Ethier CR, 2016 Finite element modeling of factors influencing optic nerve head deformation due to intracranial pressure. Invest. Ophthalmol. Vis. Sci 57, 1901–1911. [PubMed: 27088762]

Girard MJA, Beotra MR, Chin KS, Sandhu A, Clemo M, Nikita E, Kamal DS, Papadopoulos M, Mari JM, Aung T, others, 2016 In vivo 3-dimensional strain mapping of the optic nerve head following intraocular pressure lowering by trabeculectomy. Ophthalmology 123, 1190–1200. [PubMed: 26992836]

Girard MJA, Suh J-KF, Bottlang M, Burgoyne CF, Downs JC, 2009 Scleral biomechanics in the aging monkey eye. Invest. Ophthalmol. Vis. Sci 50, 5226–5237. [PubMed: 19494203]

Jonas JB, Xu L, 2014 Histological changes of high axial myopia. Eye 28, 113–117. [PubMed: 24113300]

Ma Y, Pavlatos E, Clayson K, Kwok S, Pan X, Liu J, 2020 Three-Dimensional Inflation Response of Porcine Optic Nerve Head Using High-Frequency Ultrasound Elastography. J. Biomech. Eng 142.

Ma Y, Pavlatos E, Clayson K, Pan X, Kwok S, Sandwisch T, Liu J, 2019 Mechanical Deformation of Human Optic Nerve Head and Peripapillary Tissue in Response to Acute IOP Elevation. Invest. Ophthalmol. Vis. Sci 60, 913–920. [PubMed: 30835783]

Midgett DE, Pease ME, Jefferys JL, Patel M, Franck C, Quigley HA, Nguyen TD, 2017 The pressure-induced deformation response of the human lamina cribrosa: analysis of regional variations. Acta Biomater. 53, 123–139. [PubMed: 28108378]

Midgett DE, Jefferys JL, Quigley HA, Nguyen TD, 2020 The inflation response of the human lamina cribrosa and sclera: Analysis of deformation and interaction. Acta Biomater. 106:225–241. [PubMed: 32044458]

Morgan WH, Yu DY, Cooper RL, Alder VA, Cringle SJ, Constable IJ, 1995 The influence of cerebrospinal fluid pressure on the lamina cribrosa tissue pressure gradient. Invest Ophthalmol Vis Sci 36(6):1163–72. [PubMed: 7730025]

Nguyen C, Cone FE, Nguyen TD, Coudrillier B, Pease ME, Steinhart MR, Oglesby EN, Jefferys JL, Quigley HA, 2013 Studies of scleral biomechanical behavior related to susceptibility for retinal

ganglion cell loss in experimental mouse glaucoma. Invest. Ophthalmol. Vis. Sci 54, 1767–1780. [PubMed: 23404116]

Nickells RW, Howell GR, Soto I, John SWM, 2012 Under pressure: cellular and molecular responses during glaucoma, a common neurodegeneration with axonopathy. Annu. Rev. Neurosci 35, 153–179. [PubMed: 22524788]

Norman RE, Flanagan JG, Sigal IA, Rausch SMK, Tertinegg I, Ethier CR, 2011 Finite element modeling of the human sclera: influence on optic nerve head biomechanics and connections with glaucoma. Exp. Eye Res 93, 4–12. [PubMed: 20883693]

Palko JR, Morris HJ, Pan X, Harman CD, Koehl KL, Gelatt KN, Plummer CE, Komaromy AM, Liu J, 2016 Influence of age on ocular biomechanical properties in a canine glaucoma model with ADAMTS10 mutation. PLoS One 11.

Park H-YL, Jeon SH, and Park CK, 2012 Enhanced depth imaging detects lamina cribrosa thickness differences in normal tension glaucoma and primary open-angle glaucoma. Ophthalmology 119(1): 10–20. [PubMed: 22015382]

Park H-YL, Lee NY, Choi JA, Park CK, 2014 Measurement of scleral thickness using swept-source optical coherence tomography in patients with open-angle glaucoma and myopia. Am. J. Ophthalmol 157, 876–884. [PubMed: 24412142]

Pavlatos E, Chen H, Clayson K, Pan X, Liu J, 2018a Imaging Corneal Biomechanical Responses to Ocular Pulse Using High-Frequency Ultrasound. IEEE Trans. Med. Imaging 37, 663–670. [PubMed: 29408793]

Pavlatos E, Ma Y, Clayson K, Pan X, Liu J, 2018b Regional Deformation of the Optic Nerve Head and Peripapillary Sclera During IOP Elevation. Invest. Ophthalmol. Vis. Sci 59, 3779–3788. [PubMed: 30046819]

Pavlatos E, Perez BC, Morris HJ, Chen H, Palko JR, Pan X, Weber PA, Hart RT, Liu J, 2016 Three-Dimensional Strains in Human Posterior Sclera Using Ultrasound Speckle Tracking. J. Biomech. Eng 138, 21015.

Perez BC, Pavlatos E, Morris HJ, Chen H, Pan X, Hart RT, Liu J, 2016 Mapping 3D strains with ultrasound speckle tracking: method validation and initial results in porcine scleral inflation. Ann. Biomed. Eng 44, 2302–2312. [PubMed: 26563101]

Quigley HA, Addicks EM, Green WR, Maumenee AE, 1981 Optic nerve damage in human glaucoma: II. The site of injury and susceptibility to damage. Arch. Ophthalmol 99, 635–649. [PubMed: 6164357]

Seo JH, Kim T,-W, Weinreb RN, 2014 Lamina cribrosa depth in healthy eyes. Invest. Ophthalmol. Vis. Sci 55:1241–1250. [PubMed: 24474269]

Sigal IA, Flanagan JG, Ethier CR, 2005 Factors influencing optic nerve head biomechanics. Invest. Ophthalmol. Vis. Sci 46, 4189–4199. [PubMed: 16249498]

Sigal IA, Flanagan JG, Tertinegg I, Ethier CR, 2009 Modeling individual-specific human optic nerve head biomechanics. Part I: IOP-induced deformations and influence of geometry. Biomech. Model. Mechanobiol 8, 85–98. [PubMed: 18309526]

Sigal IA, Yang H, Roberts MD, Burgoyne CF, Downs JC, 2011 IOP-induced lamina cribrosa displacement and scleral canal expansion: an analysis of factor interactions using parameterized eye-specific models, Invest Ophthalmol Vis Sci 52(3):1896–907. [PubMed: 20881292]

Sigal IA, Yang H, Roberts MD, Grimm JL, Burgoyne CF, Demirel S, Downs JC, 2011 IOP-induced lamina cribrosa deformation and scleral canal expansion: independent or related? Invest Ophthalmol Vis Sci 52(12):9023–32. [PubMed: 21989723]

Sigal IA, Grimm JL, Jan N-J, Reid K, Minckler DS, Brown DJ, 2014 Eye-specific IOP-induced displacements and deformations of human lamina cribrosa. Invest. Ophthalmol. Vis. Sci 55, 1–15. [PubMed: 24334450]

Tang J, Liu J, 2012 Ultrasonic measurement of scleral cross-sectional strains during elevations of intraocular pressure: method validation and initial results in posterior porcine sclera. J. Biomech. Eng 134, 91007.

Tehrani S, Johnson EC, Cepurna WO, Morrison JC, 2014 Astrocyte processes label for filamentous actin and reorient early within the optic nerve head in a rat glaucoma model. Invest. Ophthalmol. Vis. Sci 55, 6945–6952. [PubMed: 25257054]

Turner DC, Girkin CA, Downs JC, 2019 The magnitude of intraocular pressure elevation associated with eye rubbing. Ophthalmology 126, 171–172. [PubMed: 30153437]

Wang B, Tran H, Smith MA, Kostanyan T, Schmitt SE, Bilonick RA, Jan N-J, Kagemann L, Tyler-Kabara EC, Ishikawa H, others, 2017 In-vivo effects of intraocular and intracranial pressures on the lamina cribrosa microstructure. PLoS One 12, e0188302. [PubMed: 29161320]

Wei J, Yang B, Voorhees AP, Tran H, Brazile B, Wang B, Schuman J, Smith MA, Wollstein G, Sigal IA, 2018 Measuring in-vivo and in-situ ex-vivo the 3D deformation of the lamina cribrosa microstructure under elevated intraocular pressure, in: Optical Elastography and Tissue Biomechanics V. p. 1049611.

Weinreb RN, Cook J, Friberg TR, 1984 Effect of inverted body position on intraocular pressure. Am. J. Ophthalmol 98, 784–787. [PubMed: 6507552]

Whitford C, Joda A, Jones S, Bao F, Rama P, Elsheikh A, 2016 Ex vivo testing of intact eye globes under inflation conditions to determine regional variation of mechanical stiffness. Eye Vis. 3, 21.

Yang H, Downs JC, Sigal IA, Roberts MD, Thompson H, Burgoyne CF, 2009 Deformation of the normal monkey optic nerve head connective tissue after acute IOP elevation within 3-D histomorphometric reconstructions. Invest. Ophthalmol. Vis. Sci 50, 5785–5799. [PubMed: 19628739]

Highlights

- ONH-PPT displacement difference at IOP elevation was negatively correlated with PPT thickness.
- Radial displacement decreased in the ONH region anterior to and across LC but plateaued in the region posterior to LC.
- LC may reduce the posterior displacement of ONH at IOP elevation.

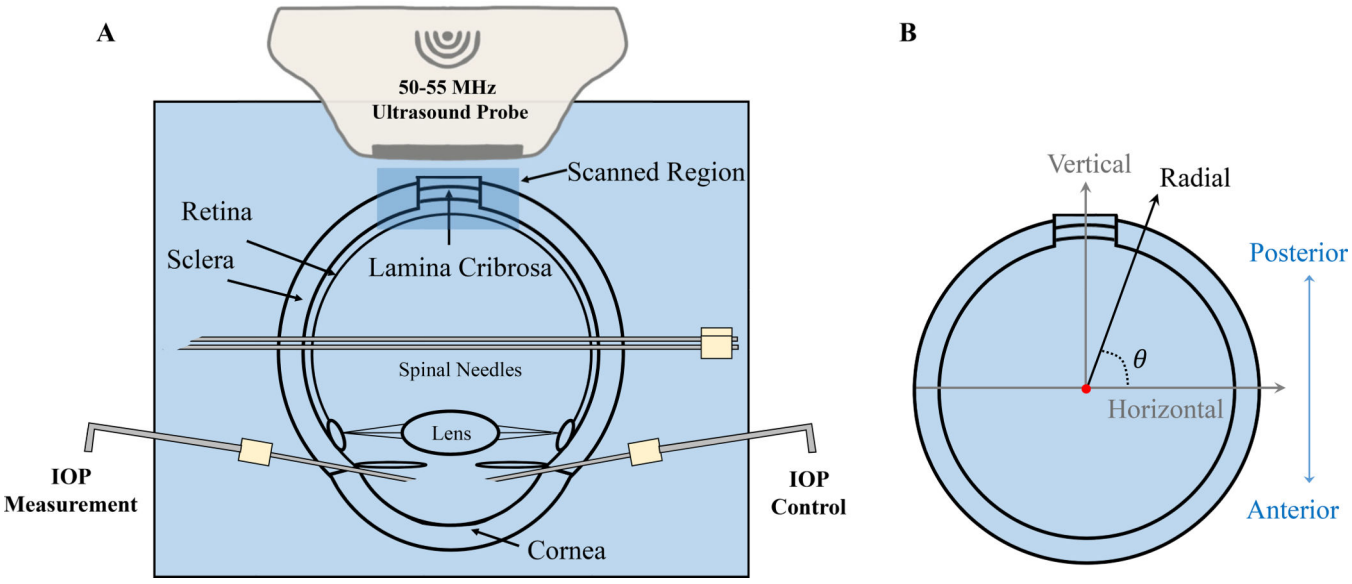

Figure 1:

A. Experimental setup for inflation testing of human donor globes with high-frequency ultrasound imaging of the ONH and surrounding PPT. **B.** The inner and outer PPT surfaces were fitted with two concentric circles. Radial displacements (displacement along globe radii) were calculated from horizontal and vertical displacements obtained from ultrasound speckle tracking along the scanning directions. Positive radial displacements indicate moving away from the globe center along the radii (outward).

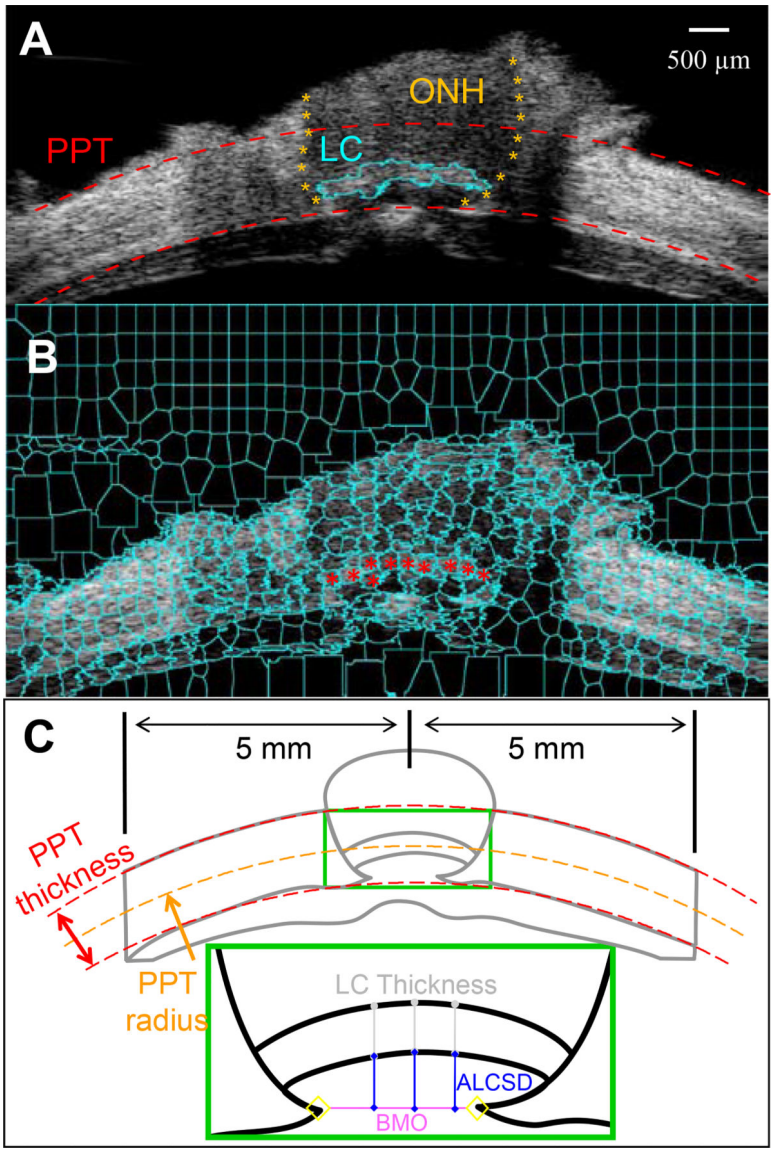

Figure 2:

A. The cross-sectional ultrasound images were manually segmented to delineate the ONH-PPT boundaries (orange asterisks) based on the differences in tissue echogenicity. The dashed red curves are circle fitted to the inner and outer PPT surfaces, which bound the ROI for displacement analysis. The retina is largely excluded from the ROI. **B.** The LC was segmented out in this eye using the superpixel method. The ultrasound image was decomposed into superpixels (cyan cells) using an automated algorithm. Superpixels belonging to the LC were manually identified (red dots). **C.** BMO was manually identified in ultrasound B-mode images. The ACLSD was calculated as the average perpendicular distance from three points (at 1/3, 1/2, and 2/3 width) on the ALCS perpendicular to the BMO reference plane. LC thickness was calculated as the average distance from the same three points to their corresponding points on the posterior LC surface.

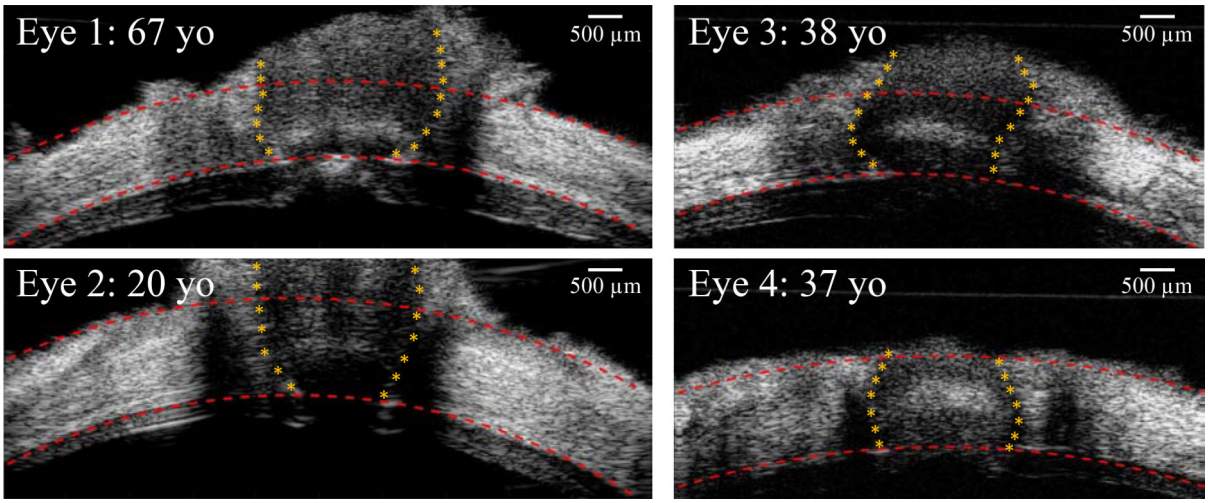

Figure 3:

B-mode images of the posterior eye from four human donors at the initial IOP (5 mm Hg), showing the variations of the ONH morphology. Images on the left column were acquired from Vevo 2100 ultrasound system with an image width of 9.73 mm, and images on the right column were from Vevo 660 with an image width of 8 mm.

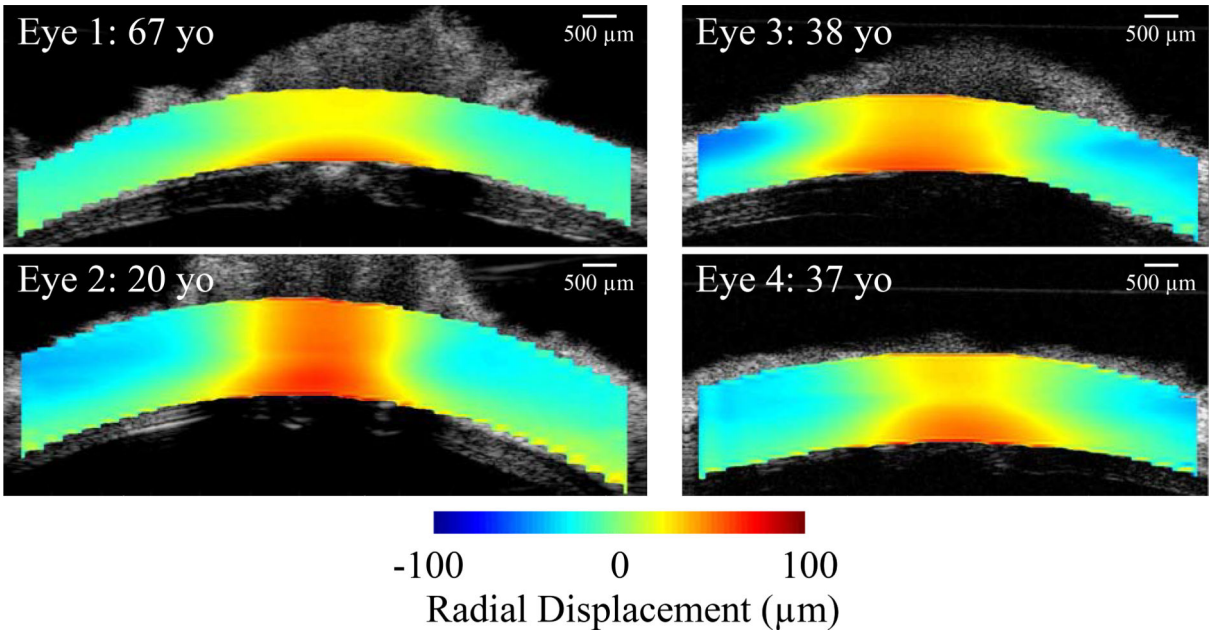

Figure 4:

Radial displacement maps at 30 mmHg are shown in four representative donor eyes. Radial displacements relative to the mean displacement of the entire ROI in each eye were plotted to better visualize the contrast between regions. The mean displacement was 44.52 µm, 88.31 µm, 77.74 µm, and 139.04 µm, for Eye 1, 2, 3, and 4, respectively. In all eyes, the ONH moved more outwardly (larger radial displacement) than the PPT.

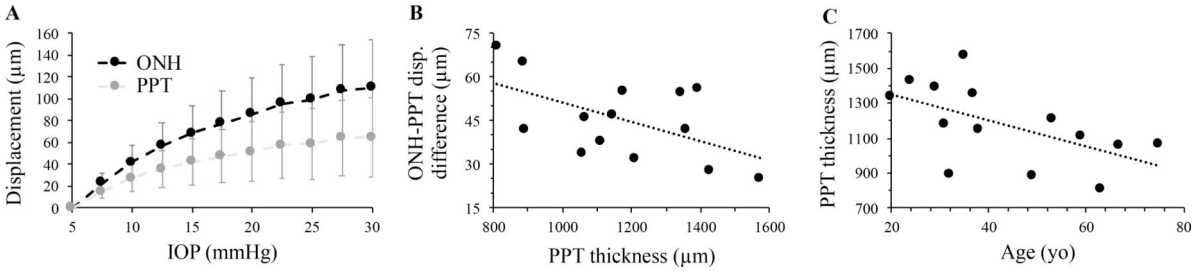

Figure 5:

A. The radial displacement of ONH and PPT increased nonlinearly with IOP; **B.** The ONH-PPT displacement difference at 30 mm Hg was negatively correlated with PPT thickness ($R = -0.55$, $p=0.041$); **C.** PPT thickness was negatively correlated with age ($R = -0.57$, $p=0.033$).

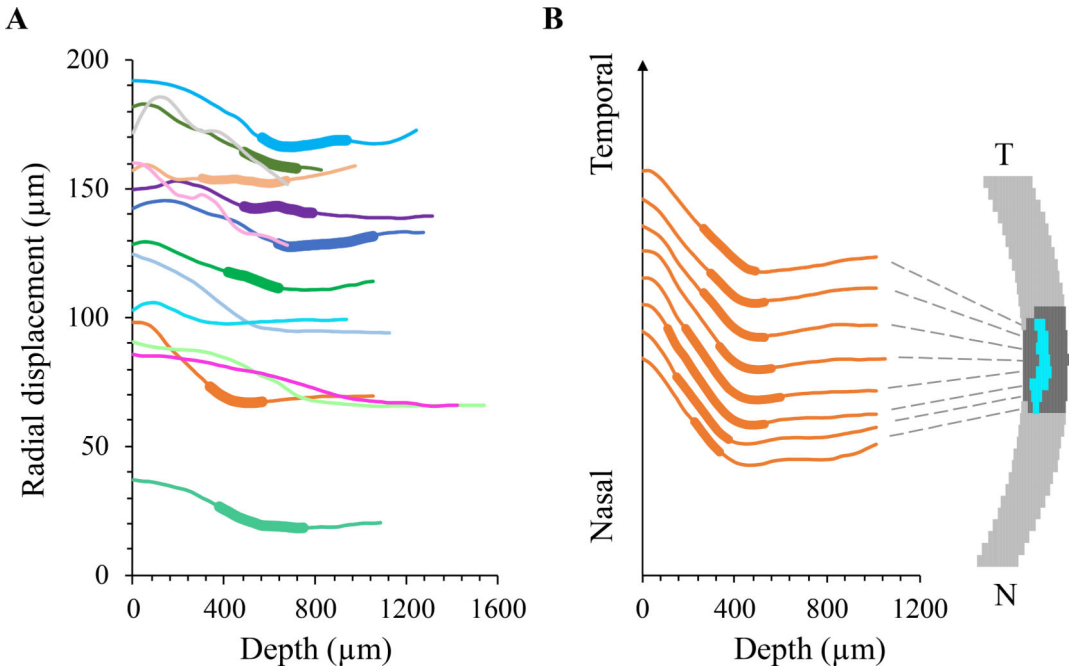

Figure 6:

A. Radial displacements in the center column of the ONH decreased from anterior to posterior ONH with a changing gradient through thickness in each tested eye (n=14, each color represents an individual eye). In eyes whose LC was identified, the LC region was indicated by a thickened segment in the curve. The LC appeared to locate at the transition region where the displacement gradient changed from negative to close the zero. **B.** Radial displacement curves from several vertical columns of the ONH in a representative eye, showing similar displacement profiles from nasal to temporal ONH. For clearer illustration, the curves were spread vertically by an equal interval at the initial point.

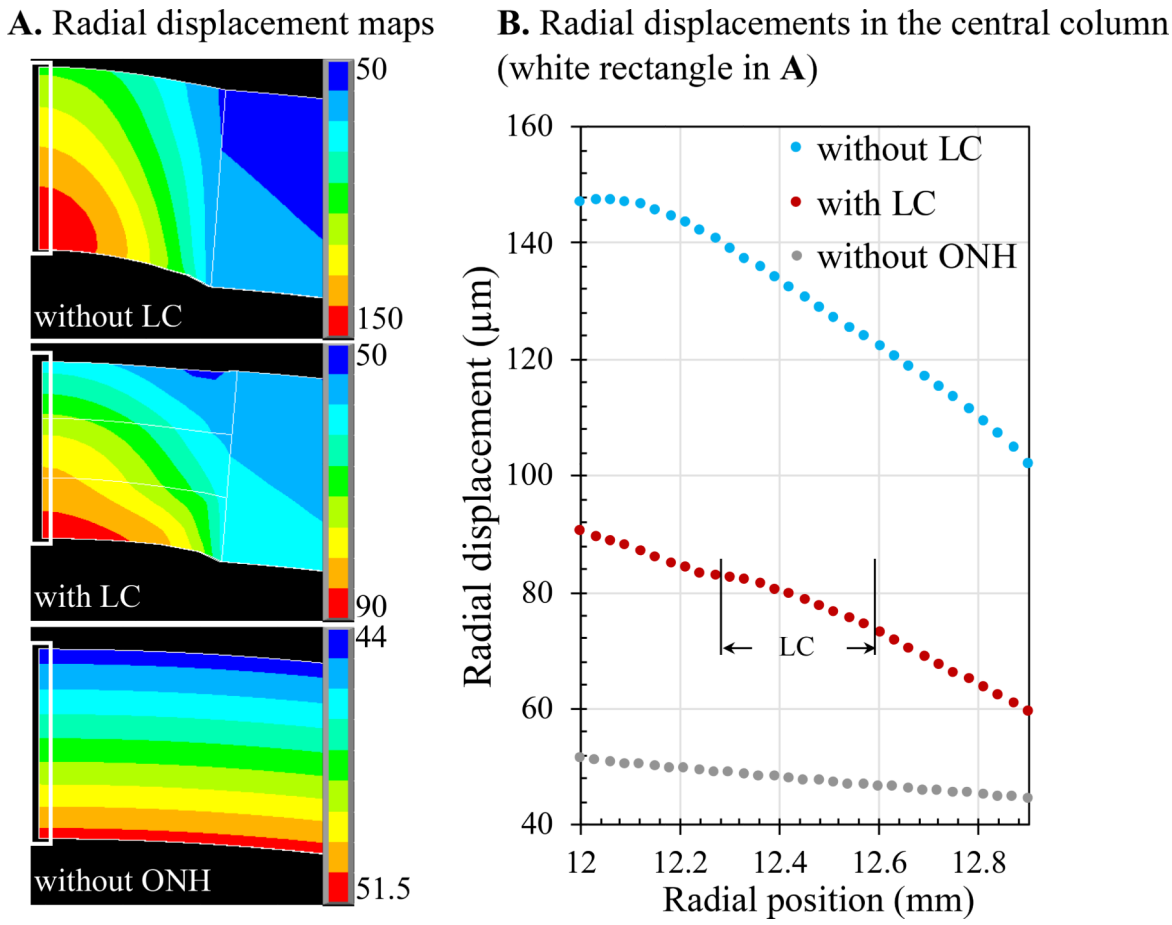

Figure 7:

Radial displacements from FE models of human posterior eye simulating a uniform scleral shell ("without ONH"), a scleral shell with an ONH but without LC ("without LC"), and a scleral shell with an ONH and an LC occupying middle third of the thickness of the ONH ("with LC"). **A.** Radial displacement maps of the posterior eye in all three scenarios. **B.** Radial displacements in the central column (white rectangle in **A**) showing that LC significantly reduced the overall displacements of the ONH; however, the simplified models did not reproduce the gradient change in the LC region observed experimentally.

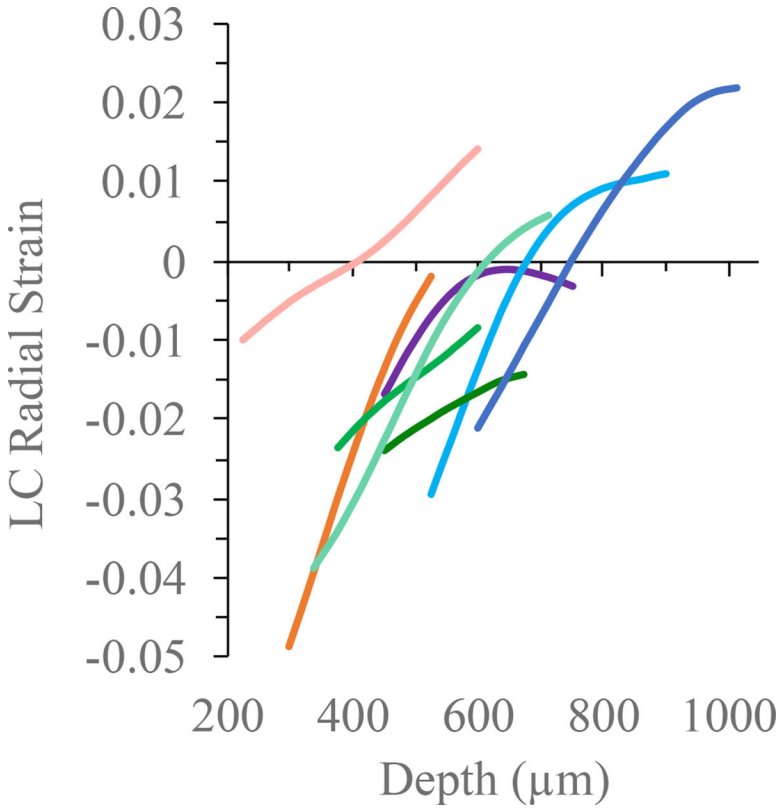

Figure 8:
Radial strain from anterior to posterior LC in the center column of the ONH in eight eyes whose LC was identified (each color represents an individual LC matching the eye's color in Figure 6). Compressive (negative) strain was highest in the anterior LC and decreased across LC. In four eyes, radial strain became positive in the posterior LC.

Table 1:

Morphological parameters and their correlations with radial displacements at 30 mmHg.

Morphological Parameter	Descriptive Statistics			Pearson Correlation Coefficients (p value)		
	Minimum	Maximum	Mean ± SD	ONH disp.	PPT disp.	ONH-PPT disp. diff.
PPT Thickness (mm; n=14)	0.81	1.57	1.17 ± 0.22	−0.33 (0.249)	−0.19 (0.515)	−0.55 * (0.041)
PPT Radius (mm; n=14)	10.65	15.94	12.50 ± 1.61	0.34 (0.234)	0.46 (0.097)	−0.13 (0.657)
Canal Size (mm; n=14)	0.98	1.77	1.38 ± 0.26	0.27 (0.350)	0.29 (0.314)	0.06 (0.838)
LC Thickness (μm; n=8)	299.50	445.50	366.75 ± 56.49	−0.13 (0.758)	−0.05 (0.906)	−0.41 (0.313)
ALCSD (μm; n=8)	295.34	670.41	476.30 ± 127.31	0.31 (0.454)	0.20 (0.634)	0.59 (0.123)

(*: statistically significant; ONH disp: ONH radial displacement; PPT disp: PPT radial displacement; ONH-PPT disp. diff.: ONH-PPT radial displacement difference)